Ocean Engineering 266 (2022) 112591

Contents lists available at ScienceDirect

Ocean Engineering

journal homepage: www.elsevier.com/locate/oceaneng

Time-optimal obstacle avoidance of autonomous ship based on nonlinear model predictive control

Ming Zhang [a], Shuai Hao [b], Defeng Wu [c], Ming-Lu Chen [d], Zhi-Ming Yuan [a,*]

[a] Department of Naval Architecture, Ocean and Marine Engineering, University of Strathclyde, 100 Montrose Street, Glasgow, G4 0LZ, UK
[b] Maritime College, Tianjin University of Technology, No. 391 Bin Shui Xi Dao Road, Tianjin, 300384, China
[c] School of Marine Engineering, Jimei University, 183, Yingjiang Road, Xiamen, 361021, Fujian, China
[d] School of Naval Architecture & Ocean Engineering, Jiangsu University of Science and Technology, 2, Mengxi Road, Zhenjiang, 212003, Jiangsu, China

ARTICLE INFO

Keywords:
Autonomous ship
Extended Kalman filter
Nonlinear model predictive control
Obstacle avoidance
Path planning
Time-optimal control
Trajectory tracking

ABSTRACT

Autonomous shipping has been identified as the way forward in the maritime transport. However, the time-optimal path planning, anti-disturbance trajectory tracking and obstacle avoidance are still ongoing challenging problems, which have not been properly addressed for autonomous ship. To fill the knowledge gap, we propose a novel nonlinear model predictive control (MPC), which integrates the time-optimal path planning, anti-disturbance tracking and obstacle avoidance. The proposed controller is designed as a 2-level hierarchical controller. In the high level, a planned path considering time minimum and obstacle avoidance is generated by nonlinear MPC in spatial formulation. A spatial reformulation is adopted to express manoeuvring time as a function mathematically. In the spatial coordinate, the manoeuvring time is minimised by MPC to generate a reference path for tracking. In the low level, vessel tracks the time-optimal planning trajectory by nonlinear MPC with extended Kalman filter in temporal formulation. The deviation of the tracking path in longitudinal direction is 15% ship length and the deviation in width direction is 1% under disturbances. The obstacle avoidance is implemented by using the proposed control method, and the tolerance of obstacle avoidance is 2*L* (ship length) to meet the safety requirement.

1. Introduction

From a total of 4104 ship accidents analysed between 2011 and 2018 (EMSA, 2019), 65.8% were attributed to human erroneous actions. 41.7% of all casualties occurred in port areas, followed by 27.4% in the coastal areas. Autonomous ships which perform tasks with little or without human interaction, can reduce the high percentage of casualties. Future progress of autonomous ships depends on the development of full autonomy, which would enable unmanned surface vehicles (USV) to work in any unstructured or unpredictable environment without human intervention (Liu et al., 2016). State-of-the-art developments of autonomous ship and auto-pilot are discussed in the Final Report and Recommendations of the manoeuvring committee to the 29th ITTC Proceeding (ITTC, 2021). The topic of unmanned navigation will be a main point of attention in the near future. Ship manoeuvrability, environmental loads, obstacles and maritime regulation should be considered when solving this problem. Studies focusing on minimising operational time during manoeuvre have been extremely rare. Hence, investigating the time-optimal ship manoeuvring problem of path planning and tracking is an engineering and academic interest.

Recent research on path planning has focused on time/ energy-minimum path, environmental loads and multi-DOF motion. Kim et al. (2017) proposed a path optimisation method using a genetic algorithm and fitness function considering environmental loads, obstacle avoidance and minimisation of travel time. Chen et al. (2019) proposed a path planning and manipulating approach based on Q-learning, which can drive a cargo ship by itself without requiring any input from human experiences. Wang et al. (2019) proposed a multilayer path planner (MPP) for a USV self-tuning path planning under complex environments. Zhao et al. (2020) applied broken straight lines instead of smooth line as reference path in practical planning application. The related studies have discussed path planning without clearly describing the manoeuvring model, thereby leaving a gap for practical application.

Trajectory tracking is an essential performance criterion for USV manoeuvring and navigation. Liu et al. (2017) developed a novel guidance and control system for a USV with environmental influences. The system was developed by integrating multiple functional modules, a robust auto-pilot module and an intelligent path planning. Huang et al. (2019) proposed a trajectory tracking controller for USVs with multiple

* Corresponding author.
E-mail addresses: ming.zhang.100@strath.ac.uk (M. Zhang), harrison@email.tjut.edu.cn (S. Hao), zhiming.yuan@strath.ac.uk (Z.-M. Yuan).

https://doi.org/10.1016/j.oceaneng.2022.112591
Received 21 March 2022; Received in revised form 13 September 2022; Accepted 14 September 2022
Available online 6 October 2022

uncertainties and input constraints. A trajectory tracking guidance law based on yaw angle and surge was used. Inner and outer disturbances were observed by reduced order extended state observers in their controller. Liao et al. (2019) discussed the berthing-oriented trajectory planning and trajectory tracking control, particularly by considering the dynamic changes of USV in berthing tasks. They used an improved fuzzy PID controller, and the control system was divided into two subsystems: heading control and speed control. In the tracking phases, reference paths are given directly without any path planning, which means path planning and tracking are based on different methodologies or techniques. The use of different methods for the two phases makes the manoeuvring control complicated and unreliable.

Obstacle avoidance is the most important ability required for USV to realise safe navigation. Woo and Kim (2020) applied a decision-making algorithm based on reinforcement learning for the path planning of surface vehicle to avoid collision in manoeuvring. Time-consuming network training and uncertainty affect limitation of the proposed method. Wang et al. (2018) proposed a path searching-based algorithm called local normal distribution-based trajectory (LNDT) based on the convention on international regulations (COLREGS) to safely avoid static and dynamic obstacles. The LNDT algorithm is only verified for single obstacle in a simulation environment. Li et al. (2021) designed a Deep Reinforce Learning to handle COLREGS collision avoidance path planning of optimal solution in the current state and simulated real-time sensor information is chosen in the practical navigation of USVs. Niu et al. (2020) proposed an energy efficient path planning algorithm under spatially–temporally environmental loads by integrating multiple algorithms. Song et al. (2018) proposed a two-level dynamic obstacle avoidance algorithm. The first level is for global planning by using the velocity obstacle algorithm and the second level is local obstacle avoidance.

Guidance–Navigation–Control (GNC) system is the brain of autonomous ship that integrates the previously discussed functionalities. Auto-pilot design is developed by different types of controllers. Gasparetto et al. (2015) presented an overview of the control algorithm of path planning and tracking. PID controller has been widely used in manoeuvring problems. In Ohtsu et al. (1996), the solutions of minimum time berthing problem was obtained by solving nonlinear two-point boundary value problems (TPBVP). However, trajectory tracking was implemented with PD controller, which is not anti-disturbance. Zhang et al. (2017) proposed a robust model predictive control used for the path-following control of surface vessel, specifically by considering roll motion in the optimisation process. Zhang et al. (2020a) applied model predictive control (MPC) for obstacle avoidance in tight environment. Mizuno et al. (2004) used ANN (Artificial Neural Network)-based nonlinear model predictive control (NMPC) to compensate for the control error of ship manoeuvring. In similar scenarios, a two-level architecture MPC controller has been widely used in obstacle avoidance and time-optimal tracking of ground vehicles (Gao et al., 2012; Frasch et al., 2013; Verschueren et al., 2014; Zhang et al., 2020a). MPC controller was adopted to solve trajectory tracking and obstacle avoidance in the fields of aerial drones and ground vehicles (Liu et al., 2020; Zhang et al., 2020b; Emami and Banazadeh, 2021). Therefore, MPC is a competitive candidate applied in GNC system with developing high-performance computation.

Time-optimal path planning, anti-disturbance trajectory tracking and obstacle avoidance are three promising topics for investigating autonomous ships. To the best of our knowledge, no study has been conducted to solve the three problems simultaneously. Moreover, integrating different methods in practical applications is unreliable and inefficient. Hence, a huge gap still exists in integrating path planning, tracking and obstacle avoidance in a powerful control system. To boost real-time autonomous control, path planning and tracking should be integrated into one control system. The present study proposes an integrated nonlinear MPC based on linear manoeuvring model for time-optimal planning and anti-disturbance tracking with obstacle avoidance. This study is inspired by the control method used for ground vehicles, and will introduce a novel spatial reformulation to optimise time consumption during ship manoeuvring operations based on a nonlinear MPC.

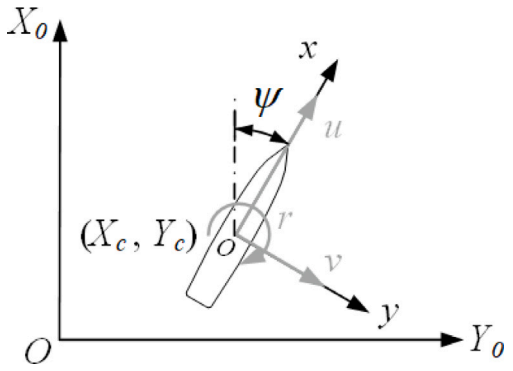

Fig. 1. Coordinate system of the manoeuvring mathematical model.

The present research proposes a novel time-optimal obstacle avoidance method based on nonlinear model predictive control. The proposed method integrates path planning, trajectory tracking and obstacle avoidance in an integrated MPC controller. With a two-level MPC architecture, path planning and tracking can be simulated in an integrated controller in a reliable and efficient manner. The integrated system promotes autonomous ship forward to real-time control. Highlights of the presented research are as follows:

(a) Introduce a spatial reformulation to mathematically solve time-optimal path planning problem,
(b) Apply nonlinear model predictive control and extended Kalman filter estimator to realise anti-disturbance trajectory tracking and
(c) Generate time-optimal planned path and track safely when obstacles exist.

The remainder of this paper is organised as follows. Section 2 introduces the mathematical manoeuvring model, which is applicable for ship manoeuvring. Section 3 presents the spatial reformulation of dynamic equation. Section 4 introduces the nonlinear MPC model and Extended Kalman filter (EKF) estimator for path planning and tracking. Section 5 discusses the simulation results of path planning and tracking for time minimum and analyses obstacle avoidance. Lastly, Section 6 presents the conclusion.

2. Mathematical manoeuvring model

The coordinate systems of ship manoeuvring motion are defined and shown in Fig. 1. A global coordinate system OX_0Y_0 is fixed on Earth, under which the trajectory of a ship is described. The other local coordinate system is fixed on the ship with the x- and y-axes pointing towards the bow and starboard, respectively. (X_c, Y_c) is the position value of origin in body-fixed coordinate in the earth-fixed coordinate. ψ is the heading angle of the vessel. u, v and r are the surge, sway and yaw velocities in the body-fixed coordinate, respectively.

Dimensionless variables are often expressed with prime superscript. However, spatial derivatives also use the same prime superscript. To avoid ambiguity, we define those spatial derivatives use the prime symbol. If there is no special explanation, then state vectors and hydrodynamic derivatives without any script are dimensionless variables based on the Froude criterion in this study. Dimensionless variables are derived by the prime system I of SNAME, as discussed in Fossen (2011).

The mathematical model of the manoeuvring motion is established on the body-fixed coordinate system. Transformation matrices are required to determine the trajectory of ship motion under the earth-fixed

coordinate system. Displacement transformation equation is expressed as follows:

$$\begin{bmatrix} X_0 \\ Y_0 \end{bmatrix} = \begin{bmatrix} \cos\psi & -\sin\psi \\ \sin\psi & \cos\psi \end{bmatrix} \begin{bmatrix} x \\ y \end{bmatrix} + \begin{bmatrix} X_c \\ Y_c \end{bmatrix}. \tag{1}$$

Moreover, the following velocity transformation equation is the derivative of Eq. (1) with respect to time:

$$\begin{bmatrix} \dot{X}_0 \\ \dot{Y}_0 \\ \dot{\psi} \end{bmatrix} = \begin{bmatrix} \cos\psi & -\sin\psi & 0 \\ \sin\psi & \cos\psi & 0 \\ 0 & 0 & 1 \end{bmatrix} \begin{bmatrix} u \\ v \\ r \end{bmatrix}, \tag{2}$$

where we add rotational motion in the horizontal plane in Eq. (2) to express the 3-degree-of-freedom (DOF) motion in an earth-fixed coordinate system.

For a control system, the propeller rotation speed and rudder angle are treated as manipulated variables (MVs). Displacements and velocities are called states. In the manoeuvring model, six states and two MVs are used to simulate the manoeuvring operation.

$$\begin{cases} X_t = \begin{bmatrix} X_0 & Y_0 & \psi & u & v & r \end{bmatrix}^{\mathrm{T}} \\ u_t = \begin{bmatrix} n_p & \delta \end{bmatrix}^{T} \end{cases}, \tag{3}$$

where X_t is the state vector and u_t is the MV vector in the temporal coordinate. The first three state vector variables are displacements in the earth-fixed coordinate system and the last three variables are velocity components in the body-fixed coordinate system. Variables of MV vector include propeller rotation speed n_p and rudder angle δ.

In this paper, we mainly focus on the advanced control method, rather than a specific application. Therefore, a 3-DOF manoeuvring model in calm water is used, which includes surge, sway and yaw. Environmental loads such as winds, waves and tides are not considered in the research. The manoeuvring equation is expressed as follows:

$$\begin{cases} m(\dot{u} - vr - x_G r^2) = F_X \\ m(\dot{v} + ur - x_G \dot{r}) = F_Y \\ (I_{zz} + mx_G^2)\dot{r} + mx_G(\dot{v} + ur) = N \end{cases}, \tag{4}$$

where m is mass of the vessel; u, v and r are the surge, sway and yaw velocities, respectively; x_G is the centre of the gravity longitudinally; I_{zz} is the moment of inertia in the horizontal plane; the superscript dot indicates the derivative with respect to the time of the corresponding quantities and F_X, F_Y and N are the external forces in the surge, sway and yaw directions, respectively. Assuming $x_G = 0$ (centre of gravity is in the mid-ship), Eq. (4) can be simplified as follows:

$$\begin{aligned} m\dot{u} - mvr &= F_X \\ m\dot{v} + mur &= F_Y \\ I_{zz}\dot{r} &= N \end{aligned}. \tag{5}$$

To solve the preceding equation system, the external forces (moments) at the right-hand side of Eq. (5) should be determined. The external force consists of three components, namely, ship hull hydrodynamic, propeller and rudder forces, which are respectively expressed as follows:

$$\begin{aligned} F_X &= X_H + X_p + X_R \\ F_Y &= Y_H + Y_p + Y_R \\ N &= N_H + N_p + N_R \end{aligned}. \tag{6}$$

where the subscripts H, p and R represent the ship hull, propeller and rudder, respectively.

A vessel often sails with cruise speed that varies in a limited range. Compared with the dominate linear components of hydrodynamic loads, nonlinear components can be disregarded. A linear manoeuvring model based on the manoeuvring model published in the 23rd ITTC Report (2002) is shown as follows:

$$\begin{cases} X_H = X_{\dot{u}}\dot{u} + X_u u \\ Y_H = Y_{\dot{v}}\dot{v} + Y_v v \\ N_H = N_{\dot{v}}\dot{r} + N_r r \end{cases}, \tag{7}$$

where $X_{\dot{u}}$, X_u, $Y_{\dot{v}}$, Y_v, $N_{\dot{v}}$ and N_r are hydrodynamic derivatives and $\dot{u}$, $\dot{v}$ and $\dot{r}$ are derivatives of u, v and r, respectively, with respect to time. Accelerations can be expressed as follows:

$$\begin{cases} \dot{u} = \frac{X_u u + mvr + X_p + X_R}{m - X_{\dot{u}}} \\ \dot{v} = \frac{Y_v v - mur + Y_R}{m - Y_{\dot{v}}} \\ \dot{r} = \frac{N_r r + N_R}{I_{zz} - N'_{\dot{v}}} \end{cases}. \tag{8}$$

Rudder forces are derived from the normal force acting on the rudder surface, as discussed in Maki et al. (2020).

$$\begin{cases} X_R = -(1 - t_R)F_N \sin\delta \\ Y_R = -(1 + a_H)F_N \cos\delta \\ N_R = -(x_R + a_H x_H)F_N \cos\delta \end{cases}, \tag{9}$$

where δ is the rudder angle; x_H is the distance between the pressure centre of the rudder and yaw centre of the hull and t_R, a_H and x_R are the reduction parameters, respectively. F_N is the normal force acting on the rudder and calculated as follows:

$$F_N = \begin{cases} \frac{1}{2}\rho A_R f_\alpha u_R^2 \sin\alpha_R & (n \geq 0) \\ 0 & (n < 0) \end{cases}, \tag{10}$$

$$\alpha_R = \delta + \frac{v + \gamma \cdot x_R \cdot r}{u_R}, \tag{11}$$

where A_R is the rudder area, α_R is the attack angle of the rudder and u_R is the flow velocity on the rudder. The flow velocity of rudder is larger than the surge velocity, which is estimated as 1.5 times the ship's surge speed u. An estimation of the attack angle can be obtained as follows:

$$\sin\alpha_R = 1.5\sin\delta. \tag{12}$$

The rudder lifting gradient coefficient f_α can be expressed as follows:

$$f_\alpha = \frac{6.13\Lambda}{2.25 + \Lambda}, \tag{13}$$

where Λ is the aspect ratio of the rudder.

Propeller forces are estimated using the propeller rotation speed (Maki et al., 2020). When propelling ahead, the propeller force can be written as follows:

$$\begin{aligned} X_p &= \begin{cases} (1 - t_{p0})\rho n_p^2 D_p^4 K_T & (n \geq 0) \\ C_3 \rho n_p^2 D_p^4 & (n < 0) \end{cases} \\ Y_p &= 0 \\ N_p &= 0 \end{aligned}, \tag{14}$$

where t_p is the thrust reduction coefficient, n_p is the propeller rotational speed, ρ is the density of water, D_p is the diameter of propeller and C_3 is a constant coefficient. The propeller thrust coefficient K_T can represented as a quadratic polynomial with respect to the propeller advance ratio J_p as follows:

$$K_T = a_1 + a_2 J_p + a_3 J_p^2, \tag{15}$$

$$J_p = \frac{(1 - w_p)u}{n_p D_p}, \tag{16}$$

where a_1, a_2, a_3 are constant coefficients and w_p is estimated as a constant value by disregarding the influence of drift angle.

It should be noted that the roll motion is not considered in the present manoeuvring model. It was found by Yoshimura (2011) that the roll motion effects on course keeping and turning abilities are remarkable when the roll motion is large, the metacentric height (GM) is low, and the ship speed is high. In the present study, the simulations are based on an ITTC benchmark model — Esso Osaka. The effects of roll motion are not archived. Therefore, we are not able to implement the roll motion into the present control model. This could potentially lead to uncertainties in the numerical simulations.

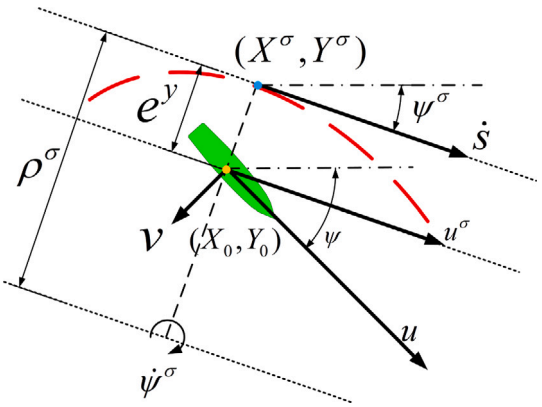

Fig. 2. Definition of the coordinate system in the spatial reformulation coordinate.

3. Spatial reformulation

The model introduced in Section 2 is the temporal hydrodynamic model, which cannot be directly used to derive the time optimal solution. Therefore, a reparameterisation is required to make the time an optimisation variable. This study proposes a novel model transformation to transform the temporal formulation to a spatial one. A curve variable is an independent variable. All states are dependent on the curve variable, including time. Time optimisation in temporal coordinate is realised approximately by numerical iteration. However, through the reformulation, the manoeuvring time is expressed clearly as a function mathematically which can be optimised in a theoretical approach.

3.1. Reference curve variable

The coordinate system used in the spatial reformulation of the ship manoeuvring model is shown in Fig. 2. (X_0, Y_0) is the coordinate in earth-fixed system. There is a point on the curve of which radius of curvature, ρ^σ, just cross through the centroid of vessel. ψ^σ is the heading angle in spatial coordinate and $\dot{\psi}^\sigma$ is its derivative. u^σ is the component along the tangential direction of curvature. $\dot{s}$ is the projection of u^σ onto the tangential line. The red dash curve $\sigma(s)$ serves as a spatial coordinate, where s is an independent variable instead of the time t. If we project the position states X_0, Y_0 and ψ from the earth-fixed coordinate $X_0 - Y_0$ onto σ, then they can be replaced by a new set of displacement states in the spatial coordinate.

$$\begin{aligned} e_y &= \cos(\psi^\sigma)(Y_0 - Y^\sigma) - \sin(\psi^\sigma)(X_0 - X^\sigma) \\ e_\psi &= \psi - \psi^\sigma \end{aligned}, \tag{17}$$

where e_y is the lateral deviation of the vessel to the reference curve, e_ψ is the rotational deviation to the reference tangential direction and X^σ, Y^σ and ψ^σ are the position states and rotational state of a reference point on the path given by the independent variable s. The manoeuvring deviation in temporal coordinate is transferred to the spatial one.

Assuming the vessel is not at rest at any time instant (i.e. $\dot{s} \neq 0$), the state vector can be expressed in the spatial coordinate. The extended state vector with the two new states can be written as follows:

$$X_s = \begin{bmatrix} X_0(s) & Y_0(s) & \psi(s) & u(s) & v(s) & r(s) & e_y(s) & e_\psi(s) \end{bmatrix}^{\mathrm{T}}, \tag{18}$$

where e_y and e_ψ are the unique state variables that are meaningful only in a spatial coordinate. Therefore, an extended state vector in a temporal coordinate is required, which can be expressed as follows:

$$X_{t,ext} = [X_t{}^{\mathrm{T}} \quad e_y(t) \quad e_\psi(t)]^{\mathrm{T}}, \tag{19}$$

where $e_y(t)$ and $e_\psi(t)$ lack a physical meaning in a temporal coordinate. However, they make the state space in the temporal and spatial coordinates be the same dimension. Thus, the state space representative in the spatial coordinate can be derived from the temporal one (Gao et al., 2012):

$$X'_s = \frac{dX'_s}{ds} = \frac{dX'_s}{dt}\frac{dt}{ds} = \frac{1}{\dot{s}}\dot{X}_{t,ext}, \tag{20}$$

where the superscript prime is used to represent the spatial derivative with respect to the curve and the superscript dot is used to represent the temporal derivative with respect to time. Velocity along the path is derived by the velocity with respect to the curve (Verschueren et al., 2014):

$$\dot{s} = \rho^\sigma \dot{\psi}^\sigma = \frac{\rho^\sigma}{\rho^\sigma - e_y}(u\cos(e_\psi) - v\sin(e_\psi)). \tag{21}$$

The derivatives of the last two state variables in Eq. (19) with respect to time are expressed as follows:

$$\begin{aligned} \dot{e}_y &= u\sin(e_\psi) + v\cos(e_\psi) \\ \dot{e}_\psi &= \dot{\psi} - \dot{\psi}^\sigma \end{aligned}. \tag{22}$$

Time consumption at each curve ds is as follows:

$$t = \frac{1}{\dot{s}}. \tag{23}$$

With the reformulation of the manoeuvring model in a spatial coordinate, total time of manoeuvring operation T, which is the optimisation target, can be written as follows:

$$T = \int_{t_0}^{t_f} 1dt = \int_{s_0}^{s_f} t ds = \int_{s_0}^{s_f} \frac{1}{\dot{s}} ds, \tag{24}$$

where the subscripts 0 and f indicate the start (lower bound) and end (upper bound), respectively, of the integration; dt is time increment in the temporal coordinate and ds is the curve increment in the spatial coordinate.

3.2. Straight-line curve simplicity

Assuming the curve is a straight line, $\rho^\sigma \gg e_y$ and $\dot{\psi}^\sigma = 0$. Thereafter, the expression of the manoeuvring model in a spatial coordinate can be simplified as follows:

$$\begin{aligned} \dot{s} &= u\cos(e_\psi) - v\sin(e_\psi) \\ \dot{e}_\psi &= \dot{\psi} \end{aligned}. \tag{25}$$

Given that these variables are involved in the majority of the state representatives, such simplification will accelerate optimisation iteration in the numerical simulations. All manoeuvring operations in this study are based on the preceding hydrodynamic equations of the MMG (Mathematical Model for Manoeuvring Ship Motion) model. With the given manoeuvring equation, a control system can be built and implemented.

4. Model predictive control

4.1. MPC algorithm

Model predictive control, as a multi-variable control method, has been increasingly applied in the field of advanced control. MPC has a simple formulation and strong optimisation capacity, which can handle the explicit model and constraints. The closed-loop control architecture of MPC is shown in Fig. 3. Dynamic optimiser, plant model, cost function and constraints are included in the controller module (Findeisen and Allgöwer, 2002) . The open-loop control (receding horizon control) inside the MPC controller is shown in Fig. 4. The plant model is a simplified estimation of actual plant which accelerates the optimisation process. The initial input of control system is random in a certain prediction horizon and import to the plant model. The initial output of the model is not-optimal. The controller will optimise the control input

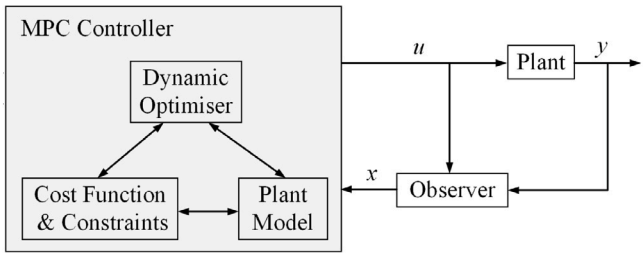

Fig. 3. Closed-loop control architecture of MPC.

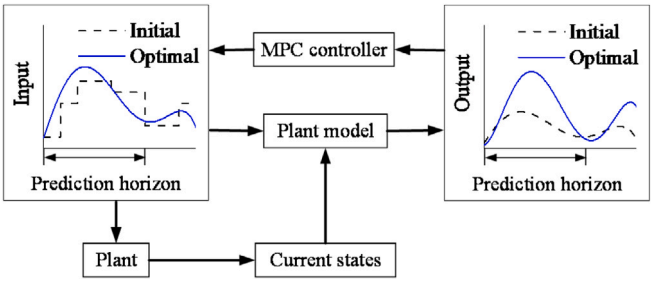

Fig. 4. Optimisation open loop of the MPC controller.

based on the defined cost function. With loops of iteration, the control input converge to the optimal one. The optimal control input imports to the actual plant to update the current state of the plant model. In the new receding horizon, the optimisation loop will repeat to generate the optimal control input in the second prediction horizon. The receding process continues until the time horizon ends. The MPC controller is design by using MATLAB Model Predictive Controller Toolbox. The main modular of numerical model is user-defined, like cost function, state space and constraints. The unmentioned modular are defined by the default setting, like dynamic optimiser.

This study will apply a nonlinear MPC to a ship manoeuvring problem owing to nonlinear nature of the low-speed manoeuvring operation. State space representative and cost function are two of the most important parts in MPC. Therefore, the following sections will expand the two parts.

4.2. State space representative

Given that states and MVs are coupled in a dynamic plant model, the state space of nonlinear MPC (Kouvaritakis and Cannon, 2016) is expressed as follows:

$$\begin{aligned} \dot{X}_t &= f_t(X_t, u_t) \\ Y_t &= h_t(X_t, u_t) \end{aligned}. \tag{26}$$

In the nonlinear MPC Toolbox of Matlab, nonlinear MPC controllers solve nonlinear programming problems using the *fmincon* function with the sequential quadratic programming (SQP) algorithm, which requires Optimisation Toolbox software. The SQP algorithm requires linearised state space to generate the optimised control input in each prediction horizon. To implement the SQP optimisation algorithm, coefficient matrices of linearised state space (A_t, B_t, C_t and D_t) can be written as follows:

$$\begin{aligned} A_t &= \frac{\partial \dot{X}_t}{\partial X_t} = \frac{\partial f_t(X_t,u_t)}{\partial X_t} \\ B_t &= \frac{\partial \dot{X}_t}{\partial u_t} = \frac{\partial f_t(X_t,u_t)}{\partial u_t} \\ C_t &= \frac{\partial Y_t}{\partial X_t} = \frac{\partial h_t(X_t,u_t)}{\partial X_t} \\ D_t &= \frac{\partial Y_t}{\partial u_t} = \frac{\partial h_t(X_t,u_t)}{\partial u_t} \end{aligned}. \tag{27}$$

The nonlinear model can be represented in a formation of linear time-invariant (LTI) state space representative as follows:

$$\begin{aligned} \dot{X}_t &= A_t X_t + B_t u_t \\ Y_t &= C_t X_t + D_t u_t \end{aligned}, \tag{28}$$

where Y_t is the observation matrix. The first equation in Eq. (28) is the description of the manoeuvring model. Observation Y_t is the same as state X_t when $C_t = \mathbf{I}$ and $D_t = \mathbf{0}$, where I is a unit matrix and 0 is a zero matrix.

Earth-fixed state variables are dependent on ψ, u, v and r. Body-fixed state variables are dependent on u, v, r and MVs. Given that not all states are coupled, we define several sub-matrices in a Jacobian matrix to simplify the expression and calculation. A_t and B_t are sparse matrices expressed as follows:

$$A_t^{6\times6} = \begin{bmatrix} 0^{3\times2} & & A_{up}^{3\times4} \\ 0^{3\times2} & 0^{3\times1} & A_{down}^{3\times3} \end{bmatrix}, \tag{29}$$

$$B_t^{6\times2} = \begin{bmatrix} 0^{3\times2} \\ B_{down}^{3\times2} \end{bmatrix}, \tag{30}$$

where

$$A_{up}^{3\times4} = \begin{bmatrix} \frac{\partial}{\partial\psi} & \frac{\partial}{\partial u} & \frac{\partial}{\partial v} & \frac{\partial}{\partial r} \end{bmatrix} \begin{bmatrix} \dot{X}_0 \\ \dot{Y}_0 \\ \dot{\psi} \end{bmatrix}, \tag{31}$$

$$A_{down}^{3\times3} = \begin{bmatrix} \frac{\partial}{\partial u} & \frac{\partial}{\partial v} & \frac{\partial}{\partial r} \end{bmatrix} \begin{bmatrix} \dot{u} \\ \dot{v} \\ \dot{r} \end{bmatrix}$$

$$B_{down}^{3\times2} = \begin{bmatrix} \frac{\partial}{\partial n_p} & \frac{\partial}{\partial \delta} \end{bmatrix} \begin{bmatrix} \dot{u} \\ \dot{v} \\ \dot{r} \end{bmatrix}. \tag{32}$$

In Eqs. (29)–(32), $A_t^{6\times6}$ is a 6×6 sparse Jacobian coefficient matrix, $A_{up}^{3\times4}$ is a 3×4 coordinate transformation matrix, $A_{down}^{3\times3}$ is a 3×3 matrix, $B_t^{6\times2}$ is a 6×2 sparse Jacobian coefficient matrix and $B_{down}^{3\times2}$ is a 3×2 matrix, which represents the manoeuvring equation. These matrices are expressed in a spatial coordinate.

Extended state vector is likewise expressed as follows:

$$\dot{X}_{t,ext} = A_{t,ext}^{8\times8} X_{t,ext} + B_{t,ext}^{8\times2} u_{t,ext}, \tag{33}$$

where $A_{t,ext}$ is an 8×8 extended Jacobian coefficient matrix of state vectors and $B_{t,ext}$ is an 8×2 extended Jacobian coefficient matrix of MV vectors. MV vector $u_{t,ext} = u_t$. The derivation of the extended state space representative in a temporal coordinate can be written as follows:

$$\begin{aligned} A_{t,ext}^{8\times8} &= \frac{\partial \dot{X}_{t,ext}}{\partial X_{t,ext}} = \begin{bmatrix} \frac{\partial \dot{X}_t}{\partial X_t} & \frac{\partial \dot{X}_t}{\partial e_y} & \frac{\partial \dot{X}_t}{\partial e_\psi} \\ \frac{\partial \dot{e}_y}{\partial X_t} & \frac{\partial \dot{e}_y}{\partial e_y} & \frac{\partial \dot{e}_y}{\partial e_\psi} \\ \frac{\partial \dot{e}_\psi}{\partial X_t} & \frac{\partial \dot{e}_\psi}{\partial e_y} & \frac{\partial \dot{e}_\psi}{\partial e_\psi} \end{bmatrix} \\ B_{t,ext}^{8\times2} &= \frac{\partial \dot{X}_{t,ext}}{\partial u_{t,ext}} = \begin{bmatrix} \frac{\partial \dot{X}_t}{\partial u_t} & \frac{\partial \dot{X}_t}{\partial u_t} & \frac{\partial \dot{X}_t}{\partial u_t} \end{bmatrix} \end{aligned} \tag{34}$$

According to Eqs. (17), (22) and (27), state space in a spatial coordinate can be expressed as follows:

$$\begin{cases} \dfrac{\partial \dot{X}_t}{\partial X_t} = A_t \\ \dfrac{\partial \dot{X}_t}{\partial e_y} = \dfrac{\partial \dot{X}_t}{\partial e_\psi} = \dfrac{\partial \dot{e}_y}{\partial e_y} = \dfrac{\partial \dot{e}_\psi}{\partial e_y} = \dfrac{\partial \dot{e}_\psi}{\partial e_\psi} = 0 \\ \dfrac{\partial \dot{e}_y}{\partial X_t} = \begin{bmatrix} 0 & 0 & 0 & \sin(e_\psi) & \cos(e_\psi) & 0 \end{bmatrix} \\ \dfrac{\partial \dot{e}_\psi}{\partial X_t} = \dfrac{\partial \psi}{\partial X_t} - \dfrac{1}{\rho^\sigma} \\ \dfrac{\partial \dot{e}_y}{\partial e_\psi} = u\cos(e_\psi) - v\sin(e_\psi) \end{cases}. \tag{35}$$

State space representative for manoeuvring model in spatial coordinate is expressed as follows:

$$X' = A_s^{8\times8} X_s + B_s^{8\times2} u_s, \tag{36}$$

where X_s is the state vector, u_s is the MV vector, A_s is an 8×8 Jacobian coefficient matrix with respect to the state vectors and B_s is an 8×2 Jacobian coefficient matrix with respect to the MV vector. By substituting Eqs. (20) and (33) into Eq. (36), the following equation is expressed as follows:

$$\begin{aligned} A_s &= \frac{\partial X'}{\partial X_s} = \frac{\partial}{\partial X_{t,ext}}\left(\frac{\dot{X}_{t,ext}}{\dot{s}}\right) \\ &= \frac{1}{\dot{s}^2}\left(\frac{\partial \dot{X}_{t,ext}}{\partial X_{t,ext}}\dot{s} - \dot{X}_{t,ext}\frac{\partial \dot{s}}{\partial X_{t,ext}}^{\mathrm{T}}\right) = \\ &\quad \frac{1}{\dot{s}^2}\left(\dot{s}A_{t,ext} - \dot{X}_{t,ext}\frac{\partial \dot{s}}{\partial X_{t,ext}}^{\mathrm{T}}\right) \\ B_s &= \frac{\partial X'}{\partial u_s} = \frac{\partial}{\partial u_s}\left(\frac{\dot{X}_{t,ext}}{\dot{s}}\right) \\ &= \frac{1}{\dot{s}^2}\left(\dot{s}\frac{\partial \dot{X}_{t,ext}}{\partial u_s} - \dot{X}_{t,ext}\frac{\partial \dot{s}}{\partial u_s}^{\mathrm{T}}\right) = \frac{B_{t,ext}}{\dot{s}} \end{aligned} \quad . \tag{37}$$

4.3. Cost function and constraints

Cost function and constraints are key components of the NMPC controller, as shown in Fig. 3. Expressions of cost function and constraints determine the optimisation process and optimal output values. We should consider the influence of states and MVs in the cost function as follows:

$$\begin{aligned} \min J(X_t, u_t) &= \min \int_{t_0}^{t_f} L(X_t, u_t)dt \\ \min J(X_s, u_s) &= \min \int_{s_0}^{s_f} L(X_s, u_s)ds \end{aligned}, \tag{38}$$

where J is the cost function, the subscripts t and s represent temporal and spatial formulations, respectively. The functionality of the MPC controller is to minimise the cost function. Meanwhile, L is the target function.

In the path planning stage, the cost function of nonlinear MPC controller is defined as time consumption of the berthing operation with constraints, which are varying ranges of state and MVs and varying ranges of their derivatives. Time consumption is expressed as a function of curve variable in spatial coordinate, as shown in Eq. (24). To minimise time consumption, cost function can be written as follows:

$$\min(J_{plan}) = \min\left(\int_{s_0}^{s_f} \frac{1}{\dot{s}}ds\right), \tag{39}$$

where J_{plan} is the cost function, which is expressed as an integral of time with respect to the curve variable and $[s_0,\ s_f]$ represents prediction horizon in a spatial coordinate.

Constraints applied at the path planning stage are defined as follows:

$$\begin{aligned} X' &= A_s X_s + B_s u_s \\ X_s &\in [X_{s,l}, X_{s,u}] \\ u_c &\in [u_{s,l}, u_{s,u}] \\ u'_c &\in [u'_{s,l}, u'_{s,u}] \\ X_s(0) &= X_{s,initial} \end{aligned} \quad . \tag{40}$$

The first constraint in Eq. (40) is state space, which represents the vessel's hydrodynamics. The second constraint corresponds to the boundary condition of the states. The subscripts l and u indicate the lower and upper bounds, respectively, of the integral. The third constraint is boundary condition of MVs. The fourth constraint is the boundary condition of the MV derivatives. The last constraint is the initial condition of the manoeuvring equation. In the trajectory tracking stage, cost function is defined as the deviation of the tracking trajectory to the planned time-optimal trajectory, which can be written as follows:

$$\min(J_{track}) = \min\left(\int_{t_0}^{t_f} \sqrt{(X_{0,track} - X_{0,ref})^2 + (Y_{0,track} - Y_{0,ref})^2}dt\right), \tag{41}$$

where X_0 and Y_0 are the positions in the earth-fixed coordinate, which is given in Eq. (3) and are elements in the first two rows of the state vector. The subscript $track$ represents the tracking states and subscript ref represents the planned states as a reference path. The initial and final conditions of the tracking trajectory are the same as the planned time-optimal one. Tracking trajectory is iteratively optimised by minimising its deviation to the planned time-optimal trajectory, and there are acceptable errors between planned trajectory and tracking one.

Constraints applied at the trajectory tracking stage are defined as follows:

$$\begin{aligned} \dot{X} &= A_t X_t + B_t u_t \\ X_t &\in [X_{t,l}, X_{t,u}] \\ u_c &\in [u_{t,l}, u_{t,u}] \\ u'_c &\in [u'_{t,l}, u'_{t,u}] \\ X_t(0) &= X_{t,initial} \end{aligned} \quad , \tag{42}$$

where constraints have similar meaning as the ones used in Eq. (40). However, these constraints are based on a temporal coordinate.

Obstacle avoidance is taken into consideration in the path planning stage. The obstacle location is treated as location constraints to avoid obstacle. As the same as the state space constraints above, the obstacle constraints need to be transformed to the spatial coordinate.

4.4. Extended Kalman filter estimation

Actions of actuators are control inputs generated by NMPC optimiser and measurements of observers are the inputs of the NMPC system gained by sensors. They are influenced by facilities' uncertainties in practical application. Hence, the manipulated action or observed states are not the accurate values. Extended Kalman filter (EKF) estimation is used in tracking simulation to reduce the influence of noise of actuators and observers. The EKF estimation preprocess the observed signal of updated states to make the measured data close to the real data based on the statistics theory. The EFK estimation makes the control system efficient and reliable. Without the EFK, there is more possibility to deviate from the optimal planned path. Given that tracking simulation is temporal discrete, EKF estimation is represented in discrete-time formation. Discrete-time state space with noise in the tracking stage is shown as follows:

$$\begin{aligned} X_k &= f(X_{k-1}, u_k) + w_k \\ Y_k &= h(X_{k-1}, u_k) + v_k \end{aligned}, \tag{43}$$

where the subscript k is time-discrete step number of current moment and $k-1$ indicates the last time step. w_k and v_k are noises of the process and observation, respectively.

$$\begin{aligned} w_k &\sim N(0, Q_k) \\ v_k &\sim N(0, R_k) \end{aligned}, \tag{44}$$

where noises are assumed to be zero mean multi-variate Gaussian noises with covariance Q_k and R_k, respectively. At each time step, the Jacobian is evaluated with current predicted states. These matrices can be used in the Kalman filter equations. This process linearises the nonlinear function around the current estimate. Notation $\hat{X}_{n|m}$ represents the estimate of the X value at time step n, which is estimated at time step m ($m \le n$). The prediction of variables is as follows:

$$\begin{aligned} \hat{X}_{k|k-1} &= f(\hat{X}_{k-1|k-1}, u_k) \\ P_{k|k-1} &= F_k P_{k-1|k-1} F_k^{\mathrm{T}} + Q_k \end{aligned}, \tag{45}$$

where $\hat{X}_{k|k-1}$ and $P_{k|k-1}$ are the predicted state and predicted covariance estimates, respectively. Updating of variables is shown as follows:

$$\begin{aligned} \tilde{y}_k &= Y_k - h(\hat{X}_{k-1|k-1}, u_k) \\ S_k &= H_k P_{k|k-1} H_k^{\mathrm{T}} + R_k \\ K_k &= P_{k|k-1} H_k^{\mathrm{T}} S_k^{-1} \\ \hat{X}_{k|k} &= \hat{X}_{k|k-1} + K_k \tilde{y}_k \\ P_{k|k} &= (I - K_k H_k) P_{k|k-1} \end{aligned} \quad , \tag{46}$$

where $\tilde{y}_k$ is the measurement residual, S_k is the residual covariance, K_k is the Kalman gain, $\hat{x}_{k|k}$ is the updated state estimate and $P_{k|k}$ is the

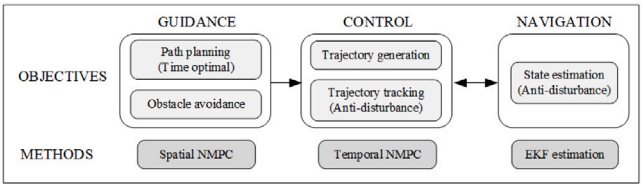

Fig. 5. Proposed objectives and methods of the GNC system.

Fig. 6. Esso Osaka tanker (1973–1985).

updated covariance estimate. Moreover, F_k and H_k are the derivatives to the state vector as follows:

$$F_k = \left.\frac{\partial f}{\partial X}\right|_{\hat{X}_{k-1|k-1},u_k}, \qquad H_k = \left.\frac{\partial h}{\partial X}\right|_{\hat{X}_{k-1|k-1},u_k} \tag{47}$$

The six states assumed to be accessible from the onboard navigation system. The six states are measured and processed by the EKF estimation before feed the data to the controller. The control system can also handle the problem if not all the states are supervised. The cases with only three states (only earth-fixed ones or only body-fixed ones) will be discussed to ensure that the controller of EFK estimation is robustness.

5. Case study and discussion

Combining the methods discussed in Sections 2 to 4, a full view of the GNC system is illustrated in Fig. 5. NPMC in spatial coordinate is used to generate the time-optimal path. The controller manipulates the rudder and propeller to track the planned path as reference using temporal NMPC. An EKF estimation will reduce the deviation caused by disturbances.

5.1. Description of the ship, rudder and propeller model

The ship model used in the numerical case study is an Esso Osaka Tanker model. The full-scale ship is shown in Fig. 6. The detailed information of the model and some essential model testing data are available in the 23rd ITTC Report (2002). Principal particulars of the dimensionless model are shown in Table 1.

Moment of inertia in the horizontal plane is estimated using the empirical formula $I_{zz} = m\cdot(0.25L_{BP})^2$. Linear hydrodynamic derivatives of the ship model are shown in Table 2. Rudder and propeller quantities are shown in Tables 3 and 4.

To validate the feasibility of the manoeuvring model, the present calculations of a standard turning circle motion and zig-zag test are compared to the experimental data from the 23rd ITTC Report (2002).

Table 1
Principle particulars of the ship model.

Principle particular, Symbol	Value
Ship length, L	1
Ship breadth, B	0.1631
Ship draft, T	0.0668
Block coefficient, C_b	0.83
Mass, m	0.0181
Moment inertia in x–y plane, I_{zz}	0.0011

Table 2
Dimensionless linear hydrodynamic used in the numerical model.

Dimensionless linear hydrodynamic	Value
$X_{\dot{u}}$	-1.81×10^{-3}
$Y_{\dot{v}}$	-1.71×10^{-2}
$N_{\dot{r}}$	-1.1×10^{-3}
X_u	-3.00×10^{-3}
Y_v	-3.92×10^{-2}
N_v	-3.00×10^{-3}

Table 3
Rudder coefficients used in the numerical model.

Rudder coefficients	Value
t_R	0.1900
a_H	0.3930
x_R	−0.5
x_H	−0.1
A_R	0.0013
Λ	3

Table 4
Propeller coefficients used in the numerical model.

Propeller coefficients	Value
t_{p0}	0.2200
D_p	0.0840
a_1	0.3278
a_2	−0.3223
a_3	−0.1560
C_3	−0.2510
w_p	0.6140

As shown in Fig. 7, the turning circle trajectory obtained by the present manoeuvring model generally agrees well with that from the experiments. The diameter of the turning circle motion is below 2.5 times the ship length, indicating that the Esso Osaka Tanker has very good turning ability. Validation shows that the present manoeuvring model is reliable. A control algorithm can be built on it to simulate complex manoeuvring operations.

We applied the parameter when the CG is located in the midship. To quantify the effects of CG on ship's trajectory, another set of data, of which the CG is not in the midship, is applied in the simulation. Table 5 compares the hydrodynamic derivatives of these two cases. Obviously, only Y_v and N_r are affected by the position of CG, and the difference is not remarkable when dimensionless x_G= 0.03 is adopted (Moreira et al., 2007). The results in Fig. 8 shows the location of CG is negligible on the planned trajectory.

5.2. Time-optimal path planning

The manoeuvring process will be dominated by cruise stage when the distance is considerably large. The effect of time-optimal manoeuvring manipulation will be diluted. However, if the distance is markedly

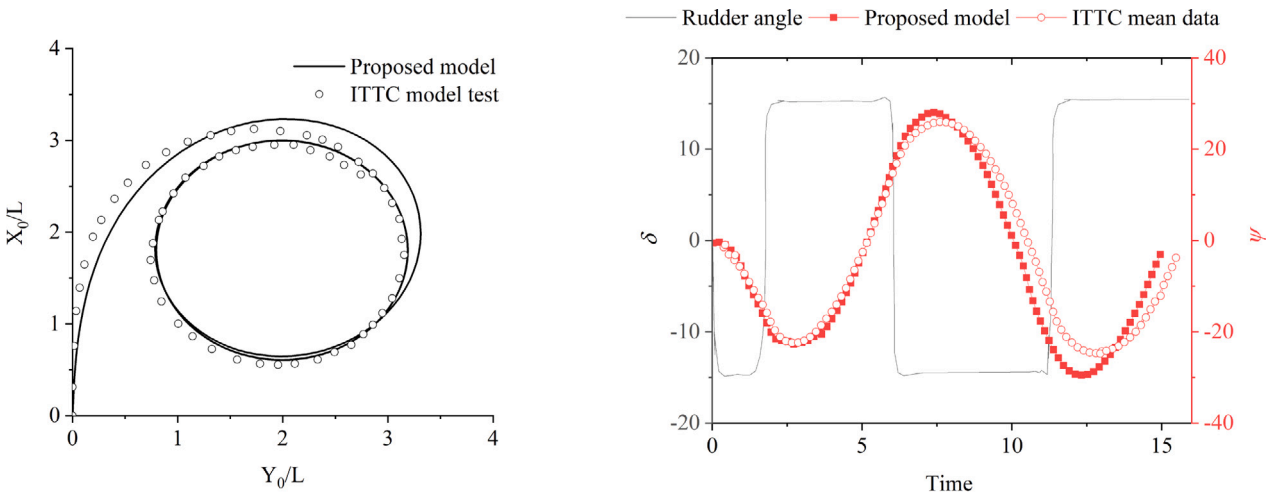

(a) Turning test simulation of the manoeuvring model. (b)

Fig. 7. Validation of proposed manoeuvring model.

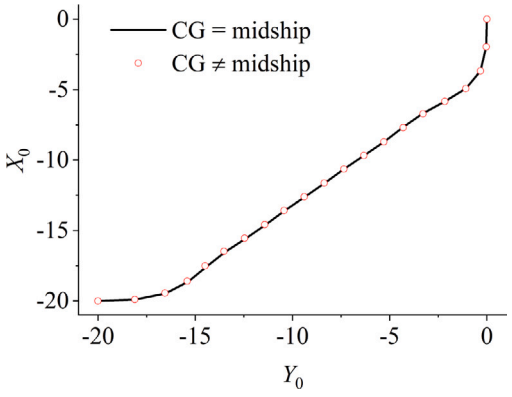

Fig. 8. Planning trajectories of time-optimal manoeuvring of two ship model.

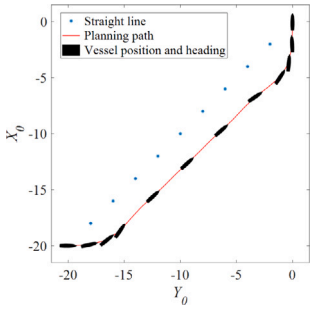

Fig. 9. Trajectory of the time-optimal path planning.

small and the vessel cannot adjust the position to the target one with limited manoeuvrability. To describe the distance clearly is important for path planning, D is introduced to measure the distance of the manoeuvring operation, which is expressed as follows:

$$\left|X_{0,initial} - X_{0,final}\right| = \left|Y_{0,initial} - Y_{0,final}\right| = D. \tag{48}$$

Table 5
Hydrodynamic derivatives measured from experimental tests.

Hydrodynamic derivatives	CG ≠ midship	CG = midship
Y_v	−0.0380	−0.0392
Y_r	0.0044	0.0056
N_v	−0.0144	−0.0144
N_r	−0.0026	−0.0030

The distance between the initial and the final positions is $\sqrt{2}D$. When comparing the manoeuvring operation at different distances, the distance needs to be nondimensionalised by D, so that it will be ranged between 0 and 1. In such case, the similarities can be summarised in the same scale. In the current study, the distance range does not fully represent scenarios from port to port directly, but it is beneficial to compare time consumption trend against simulation factors and obtain reasonable results, which will be deduced to long-distance scenarios. The initial and final conditions of the first case is defined in Table 6. The initial state indicates that the ship is heading to the positive Y_0 direction and distances are $20L$ in the X_0 and Y_0 directions. The final state indicates that the ship is required to reach a given location with zero heading angle. Surge velocity at the final moment is the same as the initial moment. The numerical result of this case is shown in Fig. 9. The blue asterisk marker is the straight line from the initial to the final position, which is the independent curve variable in spatial coordinate. The red curve is time-optimal planning trajectory, which reflects the position of the vessel. The black ship-shape sketch shows the heading angle during the manoeuvring process. Nonlinear MPC with spatial reformulation can achieve the target final states, indicating that the proposed method is fully applicable for path planning problems. As shown in Figs. 9 to 11, the manoeuvring process can be divided into three stages (i.e. initial, steady and final stages).

In the initial stage, the propeller rotation speed is the largest at the initial moment and decreases rapidly thereafter. The vessel accelerates first and propels thereafter with a constant surge velocity. The negative rudder angle causes a positive sway velocity and negative yaw rate, which keeps the vessel turned to port side until the heading angle parallels with a straight line. Given that the initial heading angle is towards the positive direction of the Y_0 axis, there is a lateral distance between the straight line and planning path after the first turning motion. During the steady stage, propeller rotation speed is a constant

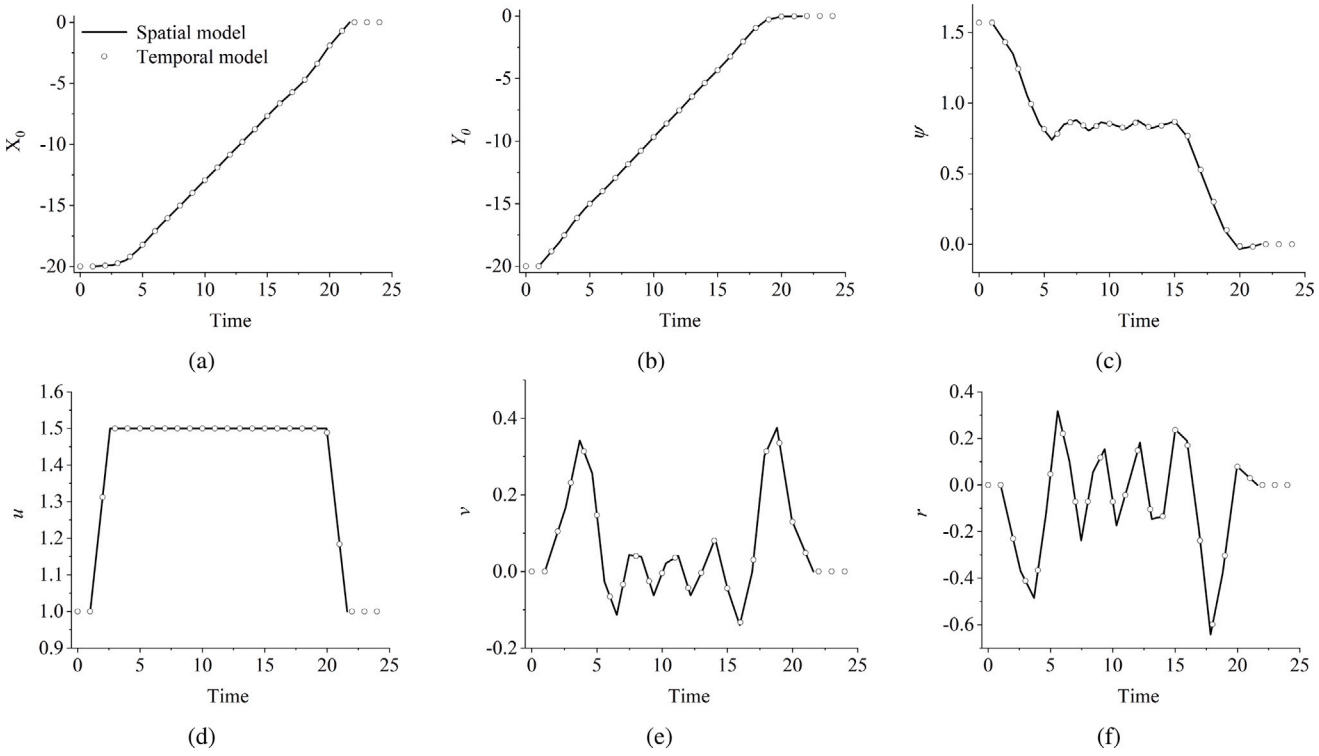

Fig. 10. State variables of the time-optimal path planning (a. displacement in X_0 direction; b. displacement in Y_0 direction; c. orientation of heading angle; d. surge velocity; e. sway velocity; f. yaw rate).

Table 6
Initial and final conditions of path planning (D = 20)

States	Initial conditions	Final conditions
X_0	20	0
Y_0	20	0
ψ	$\pi/2$	0
u	1	1
v	0	0
r	0	0

value and the rudder varies slightly close to 0. Therefore, the vessel keeps the cruise condition at maximum speed. Time consumption is mainly determined by the surge velocity u, which has a substantially larger amplitude than the sway velocity and yaw rate. Heading angle ψ equals the constant ψ^{σ}. This "steady" heading angle ψ is found when the corresponding surge velocity reaches the maximum value. Under such a circumstance, cost function of minimum time consumption can be met. In the final stage, propeller rotation speed becomes negative to decelerate, and the rudder angle is back to negative. The negative rudder angle causes a positive sway velocity and a negative yaw rate again, as previously explained. With the control manipulation, surge velocity decreases to the final required value and the vessel turns to the port side again. The displacement and heading angle reach 0 at the final moment. The time-optimal result is different from the intuitive solution which tunes the path overlapped with the straight-line path at a high-speed stage and follows the straight line. Because the final target of heading angle is on in the direction of straight line. Because the vessel needs to turn the head at the end of the operation if the vessel follows the straight line. This manipulation is consuming more time than the shown result calculated by the proposed method.

5.2.1. Influence of distance

Distance from the initial to the final position will influence the planning path sensitively. Initial and final conditions of the simulation cases are shown in Table 7. To compare the planning path fairly, displacements are normalised by dividing D as follows:

$$\begin{matrix} 0 \le X_0/D \le 1 \\ 0 \le Y_0/D \le 1 \end{matrix}, \tag{49}$$

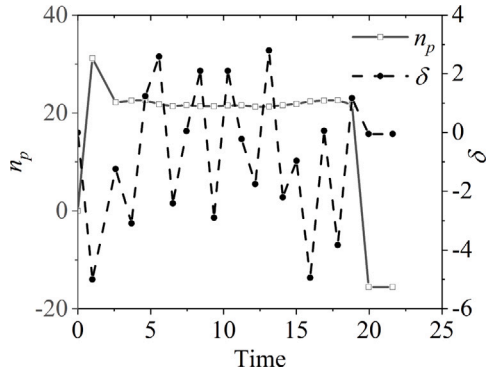

Fig. 11. Turning test simulation of the manoeuvring model.

Table 7
Initial and final conditions of path planning (D = 8, 12 and 15).

States	Initial conditions	Final conditions
X_0	D	0
Y_0	D	0
ψ	$\pi/2$	0
u	1	1
v	0	0
r	0	0

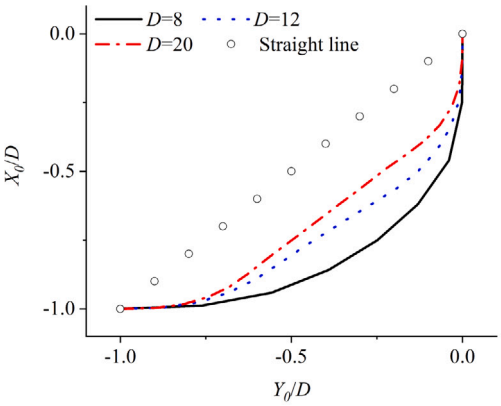

(a) Planning path trajectory.

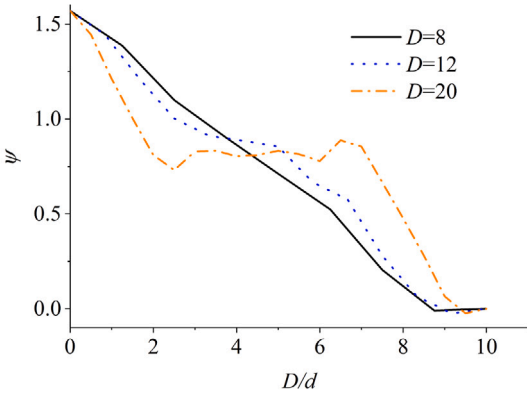

(b) Heading angle against distances.

Fig. 12. Manoeuvring manipulation in different distance cases (D/d = 10).

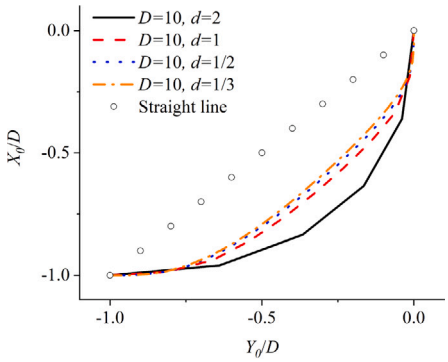

(a) D=10

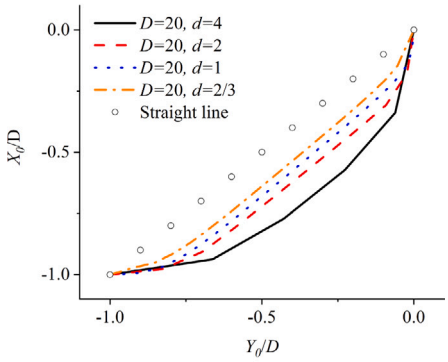

(b) D=20

Fig. 13. Planning path trajectory against the numerical increment of distance.

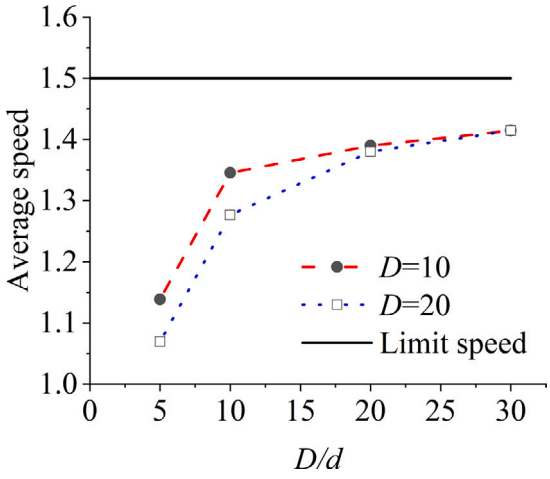

Fig. 14. Average speeds of the vessel against the numerical increment of distance.

where d is introduced to represent the spatial increment. Moreover, $\sqrt{2}d$ is the spatial increment in the numerical simulation and D/d is the step of the control horizon. Trajectories of different distances are compared in the same scale, as shown in Fig. 12(a).

A significant discrepancy exists between the long-distance cases (D = 15) and short-distance cases (D = 8). The heading angle of the short-distance case is changing continually in the entire manoeuvring process. However, the heading angle of the long-distance case keeps a constant value in the steady stage, which agrees with the case of D = 20. The case of D = 12 is the transition, in which the steady stage is short and the constant heading angle is not parallel with the straight line in Fig. 12(a). Specifically, the heading angle is larger than the straight line, which makes the vessel deviates away from the line. Lateral deviation becomes large as the vessel move forwards. The larger heading angle is influenced by the rudder force shown in Eq. (10). When the vessel decelerates (i.e. revolution of the propeller is backwards), the normal rudder force is 0, which means that the turning motion should be completed before deceleration of advance speed. This situation indicates that the vessel should turn the vessel with higher average speed in the final stage compared with that in the initial stage. Therefore, the turning radius is larger than the initial one, which can be found in the trajectory of D = 12, as shown in Fig. 12(b). When the distance is large as D = 20, the difference of the turning radius is slight in the trajectory.

5.2.2. Influence of numerical increment

The convergence of manoeuvring simulation against the numerical increment is shown in Fig. 13. Trajectories have a significant discrepancy when d decreases. When $d \leq 1$, the numerical results converge. The average speed also increases when D/d increases, as shown in Fig. 14. Curves are asymptotic to limit speed because the influences of the initial and final stages will be diluted.

5.3. Anti-disturbance trajectory tracking

As the path planning is optimised in spatial coordinate, the trajectory is not discretised by consistent time increment. Accordingly, an interpolation is implemented to generate a reference trajectory with

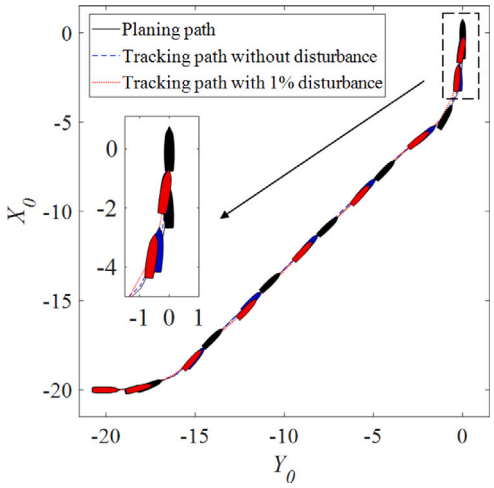

Fig. 15. Trajectories of trajectory tracking with/without disturbance (D = 20, D/d = 20).

consistent time increment. The interpolation is shown in Fig. 10. Unmeasured disturbance of actuators and observers influence the tracking path, which make path to deviate from the original planning path. Considering the unmeasured disturbance in the trajectory tracking stage, the vessel may not reach the same point of reference trajectory at the final moment of the optimal time consumption. To fill in this gap, we repeat the final state vector with an additional time duration in the interpolation process. The additional duration is 1 to 3 steps of time increments. The anti-disturbance capability of MPC and time extension can improve the performance of tracking process. The trajectory tracking process is implemented in a temporal coordinate to follow the planned time-optimal trajectory shown in Fig. 9. The results of two trajectory tracking cases are shown in Fig. 15. The dimensionless sampling time is 1 in the temporal model during the tracking stage. Deviations of the tracked trajectory to the planned one at the final moment is listed in Table 8. Displacement deviations are acceptable for trajectory tracking. The nonlinear MPC control method shows its strong anti-disturbance capability in the trajectory tracking process. State variables of time-optimal trajectory in shown in Fig. 16. In case of no disturbance, deviations of the displacements in the X_0 and Y_0 direction are $0.151L$ and $0.002L$, respectively, and the deviation of orientation is 0.004 rad. With the presence of 1% disturbance, deviation of displacements and orientation is larger than that of no disturbance case. Some residual displacements are found at the final states ($0.155L$ in the X_0 direction, $0.01L$ in the Y_0 direction and 0.012rad in the orientation direction), and the residual velocities are negligible as well. The planning simulation take minutes to generate the time-optimal trajectory on a portable workstation, Dell Precision with 8 Intel(R) Core(TM) i9-10885H CPU @ 2.40 GHz. The computational consumption is less than 60 s. The computational consumption is shorter than that of planning simulation because of the short prediction horizon. In the tracking stage, the time consumption is sensitive to the prediction horizon which is shown in Zhang et al. (2021).

To avoid singularity of cost function in the planning stage, the final surge motion is set as a non-zero value. The final states in the interpolated planned path are the constant values in the last extended increments. However, these two constraints cannot be met synchronously. The non-zero surge velocity causes that the vessel cannot be held in a position. To meet the cost function and constraints, optimisation makes the final values of all six state variables deviate to the planned path. To minimise cost function, the surge velocity at the final stage is nearly reduced to 0 m/s, and the displacement deviates from the planned one owing to residual velocities.

Table 8
Deviations of thetracking trajectory to the planning trajectory in the final moment.

States	Initial conditions	Final conditions
X_0	0.151	0.155
Y_0	0.002	−0.010
ψ	0.004	0.012
u	0.095	0.099
v	0.003	0.006
r	−0.003	−0.009

5.4. Observation selection

Six state variables are observed to track the planned path. The use of all state variables causes a trade-off among these variables because all cost functions are weighted in the cost function of tracking optimisation. Thus, all states can track with good performance. In reality, shipmasters only obtain parts of the state information, such as states in earth-fixed coordinate system received from GPS. In some special cases, body-fixed states receive more attention than earth-fixed ones. Therefore, the influence of observation selection should be discussed to guide practical navigation. Two cases are shown in Fig. 17. X_0, Y_0 and ψ are observed states in earth-fixed case as black dot curve, in which body-fixed state variables vary in flexibility. In the same manner, u, v and r are observed in body-fixed case as blue solid curve, in which earth-fixed states variables vary without constraints.

In a body-fixed case, u is tracked perfectly and the final velocity is retained as the target value, as shown in Fig. 17(d). However, displacement X_0, as shown in Fig. 17(a), must exceed the final position with $3.4L$. Only small deviations of Y_0 and ψ are present in the body-fixed case. In an earth-fixed case, there is significant deviation of u, as shown in Fig. 17(d). The final value of u is 0, which is lower than the all-state observed case. The vessel followed the same value of earth-fixed states temporally in the last increments. Therefore, the velocity must be reduced to 0 to maintain its position. The cause of influence of observation is mainly numerical interpolation and difference scheme. If the numerical simulation is sufficiently precise, there will be no differences among these cases. Considering control efficiency and capability of on-board device in practical application, observation should be selected based on navigation requirements.

5.5. Obstacle avoidance

Obstacle positions are easily reformulated because they are typically expressed in an earth-fixed spatial coordinate system. Four different cases are selected to analyse the influence of obstacles. Obstacle positions of these cases are listed in Table 9. Case 0 means no obstacle in the routine. Form cases 1 to 4, the obstacle condition becomes markedly dangerous. The obstacle position of case 1 is in the middle area with small size. The obstacle position of case 4 is close to the side with large size. Positions of obstacles and trajectory of time-optimal path are also shown in Fig. 18. Obstacle avoidance makes the planned time-optimal path deviate from that without obstacle. The consumption of manoeuvring time increases as the risk of collision increases. Tracking errors of turning motion is larger compared with the case without obstacle. Tracking paths have small curvatures, indicating a potential

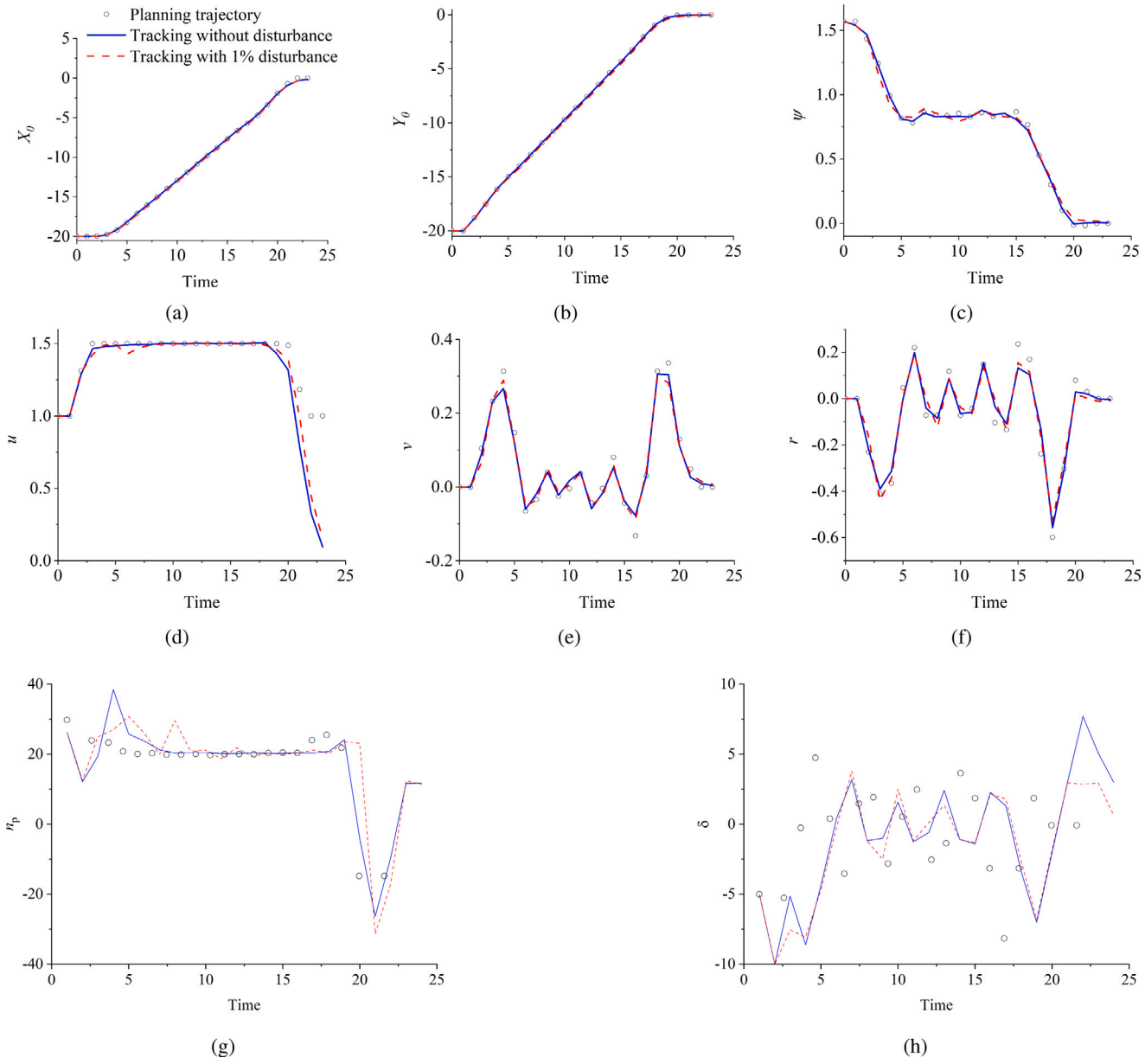

Fig. 16. State variables of time-optimal trajectory tracking, $D = 20$, $D/d = 20$, no obstacle (a. displacement in X_0 direction; b. displacement in Y_0 direction; c. orientation of heading angle; d. surge velocity; e. sway velocity; f. yaw rate; g. propeller rotation speed r; h. rudder angle).

risk of obstacle collision, which is significant in case 4. Earth-fixed state variables of planning and tracking paths with obstacle avoidance are shown in Fig. 19. Tracking paths considerably follow their corresponding planned paths in each obstacle case. When the vessel is close to an obstacle, its heading angle increases to avoid obstacles. Slope of the X_0 curve against time is slight during the steady stage and slope of the Y_0 curve at two sides of the steady stage is steeper than the case of no obstacle, as shown in Fig. 19(a). By contrast, the slope of the Y_0 curve against time is steep in the steady stage and the slope of the Y_0 curve at two sides of this period is slight, as shown in Fig. 19(b). The case where the vessel has stable heading angles has two periods: one occurs before the obstacle and the other occurs after passing the obstacle. This heading angle characteristic can be generalised to multi-obstacle scenarios. If there are N obstacles in a sufficiently long distance, then there will be $N+1$ periods with a stable heading angle. The periods of stable heading angle may be shortened or even disappeared when distance is short between obstacles, as shown in Fig. 19(c).

Table 9
Manoeuvring time of the different obstacle positions.

Obstacle case	X_0	Y_0	Time
0	None	None	20.06
1	[−11 −9]	[−9 0]	20.97
2	[10 8]	[10 0]	21.54
3	[9 7]	[11 0]	22.33
4	[8 6]	[12 0]	23.33

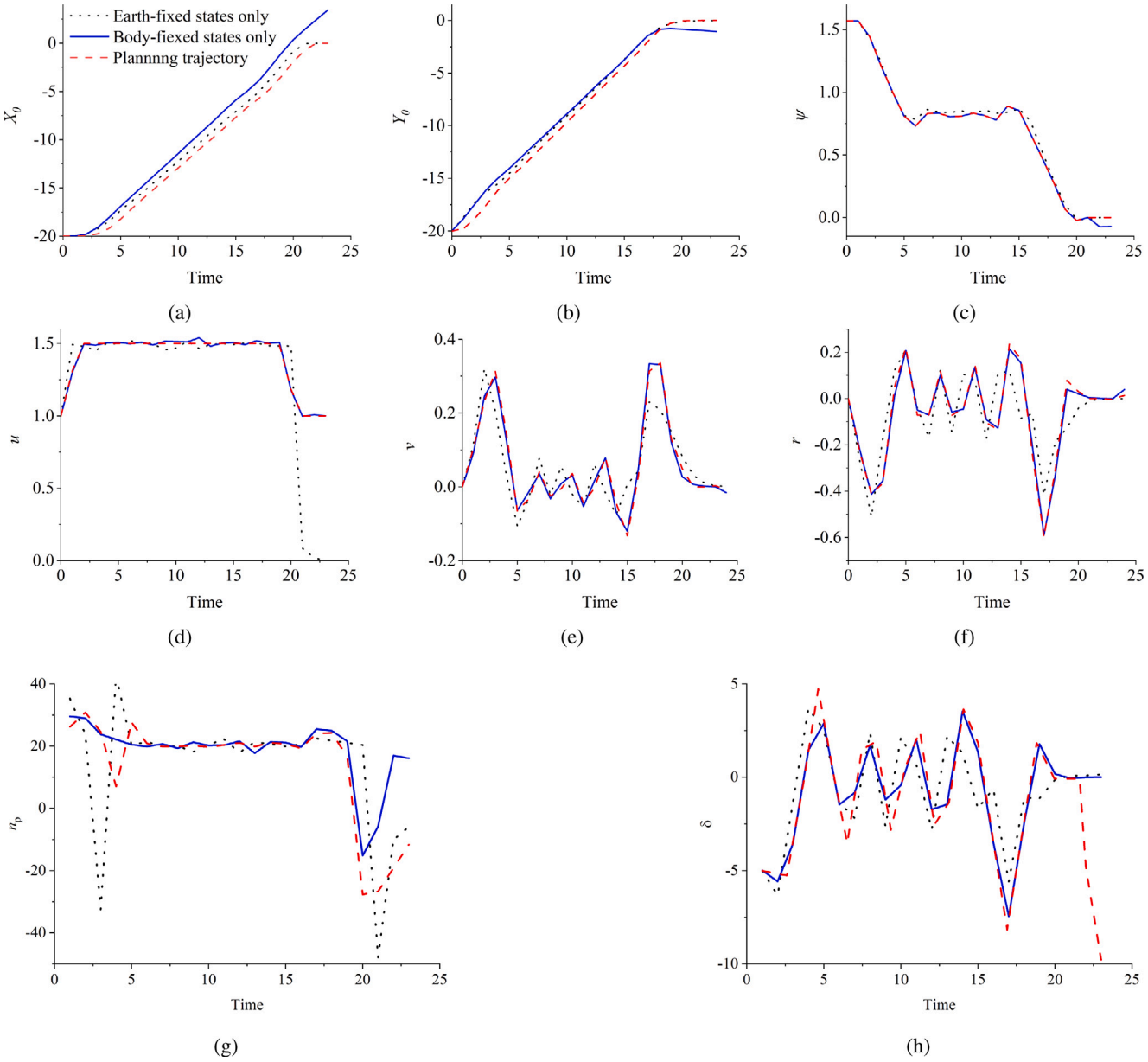

Fig. 17. State variables of time-optimal trajectory tracking with different observation states, $D = 20$, $D/d = 20$, no obstacle (a. displacement in X_0 direction; b. displacement in Y_0 direction; c. orientation of heading angle; d. surge velocity; e. sway velocity; f. yaw rate; g. propeller rotation speed r; h. rudder angle).

A risk of collision is present because the tracking error is large and ship breadth is not considered in the simulation. Setting tolerance for obstacle avoidance is important to avoid such a collision in practical manoeuvring applications. As shown in Fig. 20, if the actual obstacle is long as $10L$, then the designed obstacle in the MPC controller needs a tolerance of $2L$. This setting of tolerance effectively improves the safety of the vessel. The vessel moves across the designed obstacle and does not collide with the actual obstacle. Given that the scenario shown in Fig. 20 is the strictest case, the tolerance of $2L$ is applicable for the other cases shown in Table 9. The tolerance of $2L$ can also be used in multi-obstacle scenario, as shown in Fig. 21. Adequate gaps exist between the vessel and obstacles, and three stable heading angles are illustrated in the trajectory.

6. Conclusions

Obstacle avoidance is an ongoing challenge for autonomous ships. This study proposes a novel path planning and tracking method based on nonlinear model predictive control to solve obstacle avoidance problems in ship manoeuvring. Planned paths were optimised by introducing a spatial reformulation to represent time consumption in a spatial coordinate. Moreover, trajectory tracking was implemented based on nonlinear MPC with EKF. The behaviours of obstacle avoidance were simulated and discussed based on a non-dimensional model of the Esso Osaka tanker, in which the MMG model was applied to describe the low-speed manoeuvring motion of ships. The following conclusions can be drawn from the simulation results. (1) Nonlinear MPC with spatial reformulation is fully applicable in determining the optimal path with minimum time consumption in the path planning

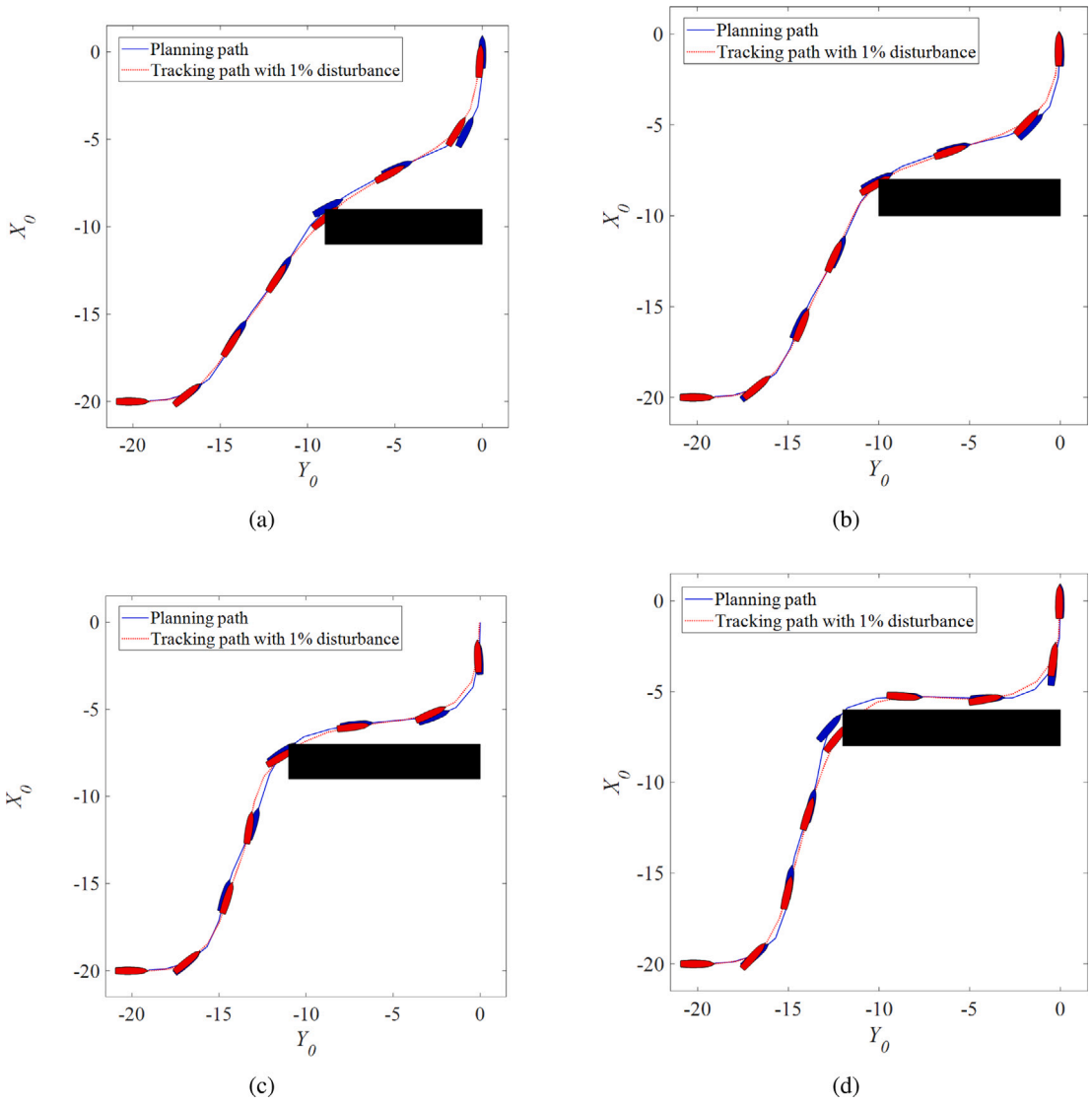

Fig. 18. Trajectories of planning and tracking paths with obstacle avoidance, $D = 20$, $D/d = 20$ (a. Obstacle case 1; b. Obstacle case 2; c. Obstacle case 3; d. Obstacle case 4).

stage. Long-distance cases have three stages in the manoeuvring process. The average speed of the vessel converges to a steady value, which is below the limited speed when the numerical increment of distance is sufficiently small. (2) Based on the nonlinear MPC and EKF estimations, trajectory tracking is implemented by considering the disturbance of observations and actuators. Selection of observation will impact tracking deviation in the final state. (3) Obstacle avoidance makes the manoeuvring time extended compared with that without obstacle. Manoeuvring behaviours are impacted by the location of obstacles. Deviations of trajectory tracking will be large in strict conditions, which could impact the safety of the manoeuvring operation. (4) Safety tolerance for the autonomous manoeuvring operation is determined as $2L$ to avoid vessel collision in the tracking stage. Safety tolerance is also applicable to multi-obstacle conditions.

CRediT authorship contribution statement

Ming Zhang: Conceptualization, Methodology, Software, Formal analysis, Investigation, Data curation, Writing – original draft, Writing – review & editing, Funding acquisition. **Shuai Hao:** Investigation, Methodology, Writing – review & editing. **Defeng Wu:** Investigation, Writing – review & editing. **Ming-Lu Chen:** Investigation, Writing – review & editing. **Zhi-Ming Yuan:** Formal analysis, Investigation, Writing – review & editing.

Declaration of competing interest

The authors declare the following financial interests/personal relationships which may be considered as potential competing interests: Ming Zhang reports financial support was provided by National Natural Science Foundation of China (51979131). Ming Zhang reports financial support was provided by China Scholarship Council Foundation (CSC201806680085).

Data availability

The authors do not have permission to share data.

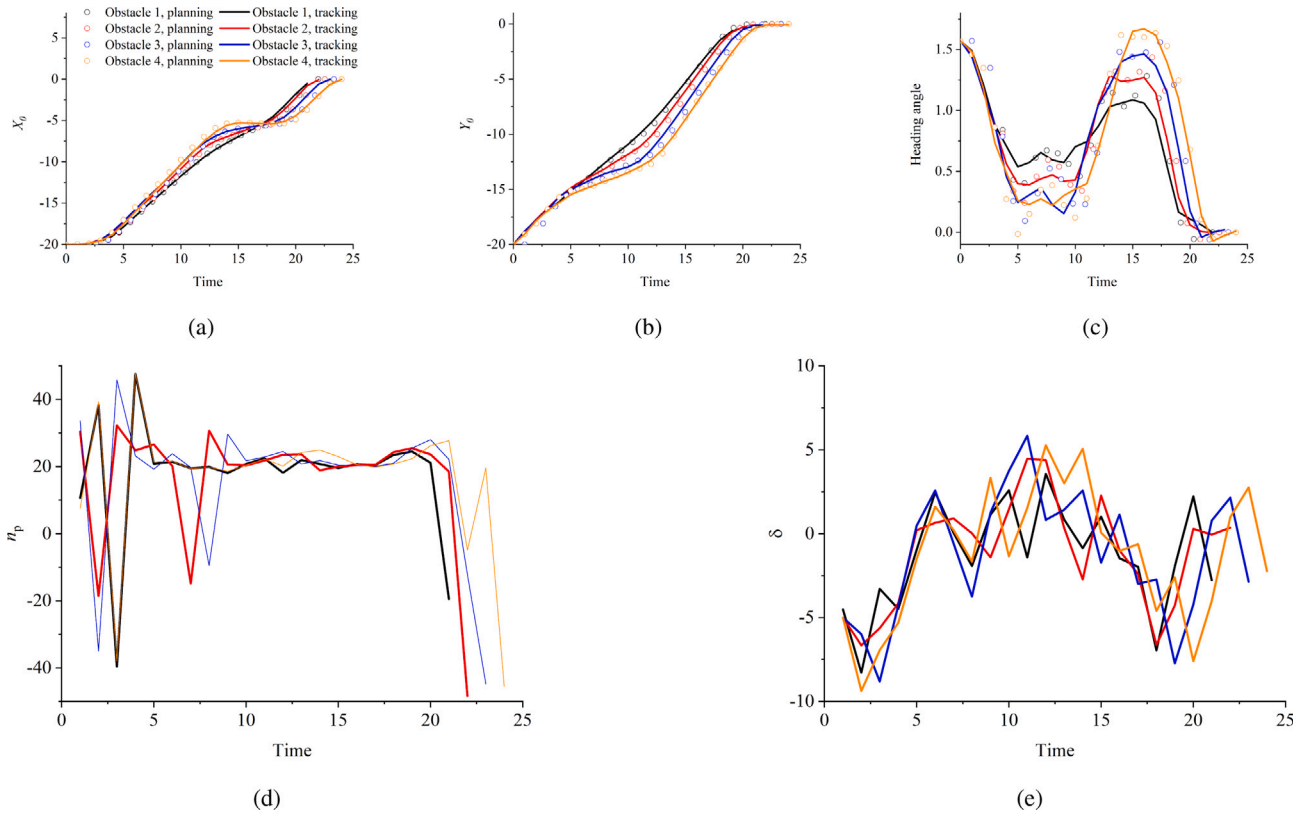

Fig. 19. Earth-fixed state variables of the planning and tracking paths with obstacle avoidance, $D = 20$, $D/d = 20$. (a. displacement in X_0 direction; b. displacement in Y_0 direction; c. orientation of heading angle; d. propeller rotation speed r; e. rudder angle).

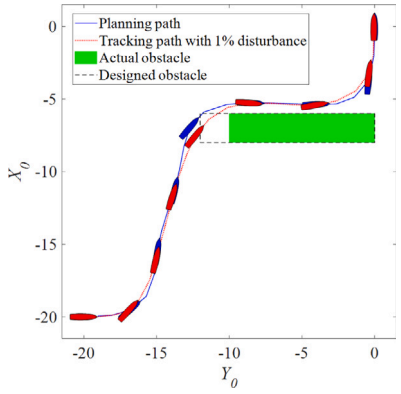

Fig. 20. Trajectories of the planning and tracking paths with single-obstacle avoidance, $D = 20$, $D/d = 20$, $d_{st} = 2$.

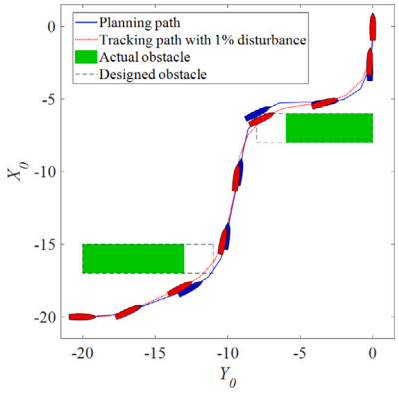

Fig. 21. Trajectories of the planning and tracking paths with multi-obstacle avoidance, $D = 20$, $D/d = 20$, $d_{st} = 2$.

Acknowledgment

This work is financially supported by National Natural Science Foundation of China (51979131) and China Scholarship Council Foundation (CSC201806680085).

References

Chen, C., Chen, X.-Q., Ma, F., Zeng, X.-J., Wang, J., 2019. A knowledge-free path planning approach for smart ships based on reinforcement learning. Ocean Eng. 189, 106299.

Emami, S.A., Banazadeh, A., 2021. Simultaneous trajectory tracking and aerial manipulation using a multi-stage model predictive control. Aerosp. Sci. Technol. 112, 106573.

EMSA, 2019. Annual Overview of Marine Casualties and Incidents 2019. Report, EMSA.

Findeisen, R., Allgöwer, F., 2002. An introduction to nonlinear model predictive control. In: 21st Benelux Meeting on Systems and Control, Vol. 11. Technische Universiteit Eindhoven Veldhoven Eindhoven, The Netherlands, pp. 119–141.

Fossen, T.I., 2011. Handbook of Marine Craft Hydrodynamics and Motion Control. John Wiley & Sons.

Frasch, J.V., Gray, A., Zanon, M., Ferreau, H.J., Sager, S., Borrelli, F., Diehl, M., 2013. An auto-generated nonlinear MPC algorithm for real-time obstacle avoidance of ground vehicles. In: 2013 European Control Conference. ECC, IEEE, pp. 4136–4141.

Gao, Y., Gray, A., Frasch, J.V., Lin, T., Tseng, E., Hedrick, J.K., Borrelli, F., 2012. Spatial predictive control for agile semi-autonomous ground vehicles. In: Proceedings of the 11th International Symposium on Advanced Vehicle Control. pp. 1–6.

Gasparetto, A., Boscariol, P., Lanzutti, A., Vidoni, R., 2015. Path planning and trajectory planning algorithms: A general overview. Mot. Opera. Plan. Robot. Syst. 3–27.

Huang, Y., Ding, H., Zhang, Y., Wang, H., Cao, D., Xu, N., Hu, C., 2019. A motion planning and tracking framework for autonomous vehicles based on artificial potential field elaborated resistance network approach. IEEE Trans. Ind. Electron. 67 (2), 1376–1386.

The Manoeuvring Committee of the 29th ITTC, 2021. The Manoeuvring Committee Final Report and Recommendations to the 29th ITTC. ITTC, URL https://ittc.info/media/9096/manoeuvring-committee.pdf.

Kim, H., Kim, S.-H., Jeon, M., Kim, J., Song, S., Paik, K.-J., 2017. A study on path optimization method of an unmanned surface vehicle under environmental loads using genetic algorithm. Ocean Eng. 142, 616–624.

Kouvaritakis, B., Cannon, M., 2016. Model predictive control. Switzerland: Springer International Publishing, p. 38.

Li, L., Wu, D., Huang, Y., Yuan, Z.-M., 2021. A path planning strategy unified with a COLREGS collision avoidance function based on deep reinforcement learning and artificial potential field. Appl. Ocean Res. 113, 102759.

Liao, Y., Jia, Z., Zhang, W., Jia, Q., Li, Y., 2019. Layered berthing method and experiment of unmanned surface vehicle based on multiple constraints analysis. Appl. Ocean Res. 86, 47–60.

Liu, Y., Bucknall, R., Zhang, X., 2017. The fast marching method based intelligent navigation of an unmanned surface vehicle. Ocean Eng. 142, 363–376.

Liu, R., Wei, M., Sang, N., 2020. Emergency obstacle avoidance trajectory tracking control based on active disturbance rejection for autonomous vehicles. Int. J. Adv. Robot. Syst. 17 (3), 1729881420921105.

Liu, Z., Zhang, Y., Yu, X., Yuan, C., 2016. Unmanned surface vehicles: An overview of developments and challenges. Annu. Rev. Control 41, 71–93.

Maki, A., Sakamoto, N., Akimoto, Y., Nishikawa, H., Umeda, N., 2020. Application of optimal control theory based on the evolution strategy (CMA-ES) to automatic berthing. J. Mar. Sci. Technol. 25 (1), 221–233.

Mizuno, N., Kuroda, M., Okazaki, T., Ohtsu, K., 2004. Minimum time ship maneuvering using neural network and nonlinear model predictive compensator. IFAC Proc. Vol. 37 (10), 297–302.

Moreira, L., Fossen, T.I., Soares, C.G., 2007. Path following control system for a tanker ship model. Ocean Eng. 34 (14–15), 2074–2085.

Niu, H., Ji, Z., Savvaris, A., Tsourdos, A., 2020. Energy efficient path planning for unmanned surface vehicle in spatially-temporally variant environment. Ocean Eng. 196, 106766.

Ohtsu, K., Shoji, K., Okazaki, T., 1996. Minimum-time maneuvering of a ship, with wind disturbances. Control Eng. Pract. 4 (3), 385–392.

Report, r.I., 2002. The Specialist Committee on Esso Osaka. Report.

Song, A.L., Su, B.Y., Dong, C.Z., Shen, D.W., Xiang, E.Z., Mao, F.P., 2018. A two-level dynamic obstacle avoidance algorithm for unmanned surface vehicles. Ocean Eng. 170, 351–360.

Verschueren, R., De Bruyne, S., Zanon, M., Frasch, J.V., Diehl, M., 2014. Towards time-optimal race car driving using nonlinear MPC in real-time. In: 53rd IEEE Conference on Decision and Control. IEEE, pp. 2505–2510.

Wang, N., Jin, X., Er, M.J., 2019. A multilayer path planner for a USv under complex marine environments. Ocean Eng. 184, 1–10.

Wang, Y., Yu, X., Liang, X., Li, B., 2018. A COLREGs-based obstacle avoidance approach for unmanned surface vehicles. Ocean Eng. 169, 110–124.

Woo, J., Kim, N., 2020. Collision avoidance for an unmanned surface vehicle using deep reinforcement learning. Ocean Eng. 199, 107001.

Yoshimura, Y., 2011. Effect of roll motion on ship manoeuvrability by a rudder to yaw response equation. J. Jpn. Soc. Naval Archit. Ocean Eng. 13, 11–18. http://dx.doi.org/10.2534/jjasnaoe.13.11.

Zhang, M., Chung, K.S., Yuan, Z.-M., 2021. Time-optimal path planning and tracking based on nonlinear model predictive control and its application on automatic berthing (under revision). IEEE Trans. Control Syst. Technol..

Zhang, X., Liniger, A., Borrelli, F., 2020a. Optimization-based collision avoidance. IEEE Trans. Control Syst. Technol..

Zhang, X., Ma, J., Cheng, Z., Huang, S., Ge, S.S., Lee, T.H., 2020b. Trajectory generation by chance-constrained nonlinear MPC with probabilistic prediction. IEEE Trans. Cybern. 51 (7), 3616–3629.

Zhang, J., Sun, T., Liu, Z., 2017. Robust model predictive control for path-following of underactuated surface vessels with roll constraints. Ocean Eng. 143, 125–132.

Zhao, Y., Qi, X., Incecik, A., Ma, Y., Li, Z., 2020. Broken lines path following algorithm for a water-jet propulsion USV with disturbance uncertainties. Ocean Eng. 201, 107118.